Mackenzie, A. Pranzo, *J. Chem. Soc. Perkin Trans. 1* **2000**, 3561; c) B. Chao, D. C. Dittmer, *Tetrahedron Lett.* **2000**, *41*, 6001.
[4] a) M. C. Elliott, C. J. Moody, T. J. Mowlem, *Synlett* **1993**, 909; b) D. S. Brown, M. C. Elliott, C. J. Moody, T. J. Mowlem, *J. Chem. Soc. Perkin Trans. 1* **1995**, 1137.
[5] For antisecretory and antihistamine activities, see: a) S. Ram, A. K. Saxena, P. C. Jain, G. K. Patnaik *Indian J. Chem. Sect. B* **1984**, *23*, 1261; b) M. W. Klohs, F. J. Petracek (Dart Industries Inc.), US Patent 3471519, **1969** [*Chem. Abstr.* **1969**, *71*, 124212].
[6] S. J. Coote, S. G. Davies, D. Middlemiss, A. Naylor, *J. Organomet. Chem.* **1989**, *379*, 81.
[7] For reviews, see: a) S. G. Davies, S. J. Coote, C. L. Goodfellow in *Advances in Metal-Organic Chemistry*, *Vol. 2* (Ed.: L. S. Liebeskind), JAI, London, **1989**, p. 1; b) S. G. Davies, T. D. McCarthy in *Comprehensive Organometallic Chemistry II*, *Vol. 12* (Eds.: E. W. Abel, F. G. A. Stone, G. Wilkinson), Pergamon, New York, **1995**, p. 979.
[8] a) H.-G. Schmalz, S. Siegel in *Transition Metals for Organic Synthesis*, *Vol. 1* (Eds.: M. Beller, C. Bolm), Wiley-VCH, Weinheim, **1998**, p. 550; b) M. Uemura in *Advances in Metal-Organic Chemistry*, *Vol. 2* (Ed.: L. S. Liebeskind), JAI, London, **1989**, p. 195.
[9] a) A. Pfletschinger, T. K. Dargel, H.-G. Schmalz, W. Koch, *Chem. Eur. J.* **1999**, *5*, 537; b) C. A. Merlic, J. C. Walsh, D. J. Tantillo, K. N. Houk, *J. Am. Chem. Soc.* **1999**, *121*, 3596.
[10] For selected recent work, see: a) F. Dehmel, H.-G. Schmalz, *Org. Lett.* **2001**, *3*, 3579; b) D. Hörstermann, H.-G. Schmalz, G. Kociok-Köhn, *Tetrahedron* **1999**, *55*, 6905; c) T. Geller, H.-G. Schmalz, J. W. Bats, *Tetrahedron Lett.* **1998**, *39*, 1537; d) K. Schellhaas, H.-G. Schmalz, J. W. Bats, *Chem. Eur. J.* **1998**, *4*, 57; e) H.-G. Schmalz, A. Majdalani, *Synlett* **1997**, 1303.
[11] a) R. A. Ewin, N. S. Simpkins, *Synlett* **1996**, 317; b) R. A. Ewin, A. M. MacLeod, D. A. Price, N. S. Simpkins, A. P. Watt, *J. Chem. Soc. Perkin Trans. 1* **1997**, 401; for a review, see: c) S. E. Gibson (née Thomas), E. G. Reddington, *Chem. Commun.* **2000**, 989.
[12] For details of the crystal structure analyses of compounds *rac*-**11d**, **11a**, *rac*-**17b**, and *rac*-**17f**, see Supporting Information. CCDC-179013 (*rac*-**11d**), CCDC-179014 (**11a**), CCDC-179015 (*rac*-**17b**), and CCDC-179016 (*rac*-**17f**) contain the supplementary crystallographic data for this paper. These data can be obtained free of charge via www.ccdc.cam.ac.uk/conts/retrieving.html (or from the Cambridge Crystallographic Data Centre, 12, Union Road, Cambridge CB2 1EZ, UK; fax: (+44) 1223-336-033; or deposit@ccdc.cam.ac.uk).
[13] D. A. Price, N. S. Simpkins, A. M. MacLeod, A. P. Watt, *J. Org. Chem.* **1994**, *59*, 1961.
[14] a) T. Volk, D. Bernicke, J. W. Bats, H.-G. Schmalz, *Eur. J. Inorg. Chem.* **1998**, 1883; b) J. Blagg, S. J. Coote, S. G. Davies, B. E. Mobbs, *J. Chem. Soc. Perkin Trans. 1* **1986**, 2257.
[15] D. J. Peterson, *Organomet. Chem. Rev. Sect. A* **1972**, 7, 295.
[16] A diastereomeric mixture of *rac*-**13** and *rac*-**11h** (7.5:1) was formed, which was easily separated by chromatography.
[17] In this case, a by-product (19%) of type **10** was obtained which indicates a strong kinetic isotope effect (abstraction of D_{endo} at C1 *versus* H_{exo} at C3).
[18] A participation of the ring oxygen atom (as a coordinating site) in the *endo* deprotonation step is likely, as other benzylic silylated [arene–$Cr(CO)_3$] complexes do not exhibit such behavior; see, for example: J. Blagg, S. J. Coote, S. G. Davies, D. Middlemiss, A. Naylor, *J. Chem. Soc. Perkin Trans. 1* **1987**, 689.
[19] For other examples of *exo*-protonation of $Cr(CO)_3$-complexed benzylic anions, see refs. [10a, e], as well as: H.-G. Schmalz, S. Siegel, D. Bernicke, *Tetrahedron Lett.* **1998**, *39*, 6683.
[20] The base **18** was prepared from *R*-(+)-1-phenylethylamine: see: N. S. Simpkins, K. Bambridge, M. J. Begley, *Tetrahedron Lett.* **1994**, *35*, 3391.
[21] The absolute configuration of **11a** was determined by X-ray crystal-structure analysis[12] and confirmed the expected results.[11b]

Chemically Tuning between Ferromagnetism and Antiferromagnetism by Combining Theory and Synthesis in Iron/Manganese Rhodium Borides**

Richard Dronskowski,* Karol Korczak, Heiko Lueken, and Walter Jung

Dedicated to Professor Welf Bronger on the occasion of his 70th birthday

Cooperative magnetic phenomena such as ferromagnetism and antiferromagnetism have not only made up an enormously rich synthetic and theoretical playground for generations of solid-state physicists and chemists,[1, 2] they also form the material basis of the most critical key technology of today's information society, namely data storage and data retrieval.[3, 4] Fortunately enough, within the last two decades modern high-level electronic-structure calculations of the density-functional type have proven to be able to reproduce a number of essential observables (e.g., magnetic moments) in many (inter)metallic magnets with satisfying accuracy, thereby offering a first step in an atomistic understanding of these magnetic properties. Only recently, however, has it been shown that a more chemically oriented theoretical framework, intended to offer semiquantitative signposts for the synthesis of new cooperative magnets, can be constructed simply by identifying bonding "fingerprints" which are characteristic for either metallic ferromagnets or antiferromagnets.[5, 6]

When a nonmagnetic ("spin-restricted") band-structure calculation is performed on a typical ferromagnet such as bcc-Fe, a crystal orbital Hamilton population (COHP) bonding analysis yields *antibonding* Fe–Fe interactions at the Fermi level (Figure 1, top left), which indicates an electronic instability. Upon spontaneous spin polarization ("spin-unrestricted" calculation), bcc-Fe undergoes a distortion, but instead of the atoms the electrons rearrange themselves.[7] Thus, spontaneous magnetization makes the spin-up (α) and spin-down (β) electrons inequivalent, thereby reducing the electronic symmetry, which annihilates the antibonding states and, consequently, lowering the overall energy and the bonding energy by a few percent (Figure 1, top right).[5, 6] For antiferromagnetism, things are a little bit more subtle. A corresponding nonmagnetic band-structure calculation on a typical antiferromagnet such as bcc-Cr results in the Fermi level being positioned exactly between the bonding and

[*] Prof. Dr. R. Dronskowski, K. Korczak, Prof. Dr. H. Lueken
Institut für Anorganische Chemie
Rheinisch-Westfälische Technische Hochschule
Professor-Pirlet-Strasse 1, 52056 Aachen (Germany)
Fax: (+49) 241-80-92288
E-mail: drons@HAL9000.ac.rwth-aachen.de
Prof. Dr. W. Jung
Institut für Anorganische Chemie
der Universität zu Köln
Greinstrasse 6, 50939 Köln (Germany)

[**] It is a pleasure to thank Dipl.-Chem. Uwe Couhorn, Dipl.-Chem. Yasemin Kurtulus, and Dr. Bernhard Eck for assistance as well as the Fonds der Chemischen Industrie for their support.

  1433-7851/02/4114-2528 $ 20.00+.50/0

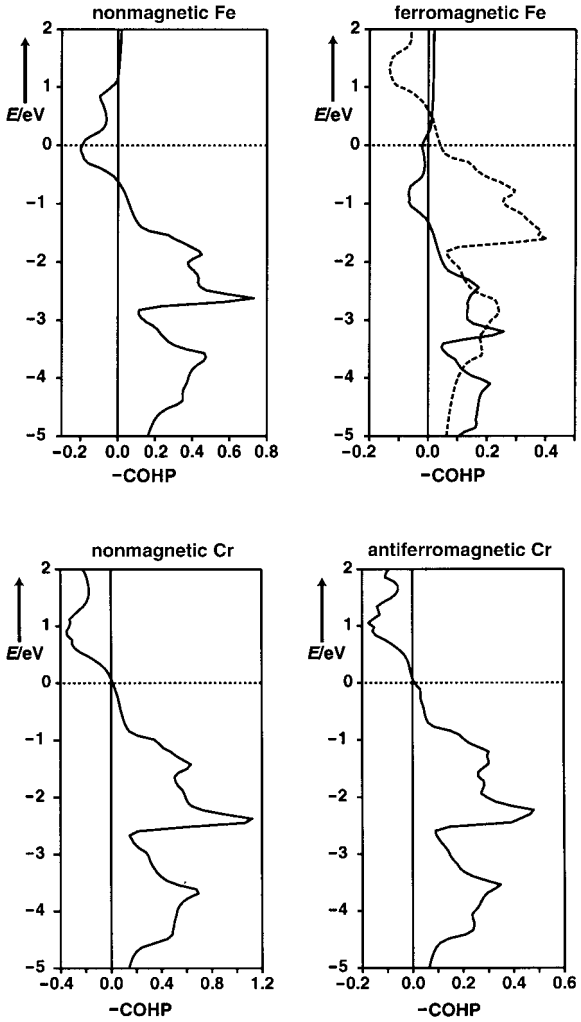

Figure 1. Top: COHP analysis of Fe–Fe bonding in nonmagnetic bcc-Fe (left) and in ferromagnetic, spin-polarized bcc-Fe (right; α spin lattice (——), β spin lattice (- - - -)). Bottom: COHP analysis of Cr–Cr bonding in nonmagnetic bcc-Cr (left) and in antiferromagnetic, spin-polarized bcc-Cr (right); the Fermi levels (horizontal dotted lines) have been set to zero.

antibonding states, that is, in the *nonbonding* region (Figure 1, bottom left). This situation does not alter very much when a real antiferromagnetic calculation is performed; the states around the Fermi level remain nonbonding, the strength of interatomic bonding stays very much the same,[6, 8] and it is only the slightly changing slope of the COHP close to the Fermi level that reminds us of a well-known instability in extended solids[9] (Figure 1, bottom right). To successfully create new metallic ferromagnets and antiferromagnets, the synthetic recipe[6, 8] for all transition metals and their alloys reads as follows: *Try to adjust the Fermi level of the material under investigation so as to position it within the antibonding states (ferromagnets) or nonbonding states (antiferromagnets) of the magnetically active atoms, that is, those atoms which have narrow band widths in their elemental forms.* Here are some examples for such a *tuning* of the valence-electron concentration by means of either an electronic enrichment or depletion:

The quaternary family of intermetallic phases $A_2MRh_5B_2$ (M = metal) which crystallize in an ordered, substitutional variant of the $Ti_3Co_5B_2$ structure type, is especially well-suited to exploit these ways of chemical thinking since the overall structure is robust enough to allow a number of chemical substitutions to take place by skillful syntheses.[10] We will discuss the structural peculiarities using the example of $Mg_2MnRh_5B_2$, an electron-poor representative of this rich family of compounds, all of which crystallize in the space group *P*4/*mbm*. Within the tetragonal unit cell (see Figure 2, left), there are trigonal, tetragonal, and pentagonal rhodium prisms stacked on top of each other along the [001] direction. While the triangular prisms are centered by boron atoms, the pentagonal prisms accommodate magnesium atoms; the tetragonal prisms contain the magnetically important manganese atoms (see also Figure 2, right). As a result, there are quasi 1D Mn–Mn chains running along the *c* axis with intrachain distances of about 2.91 Å while the interchain distances are on the order of 6.60 Å.

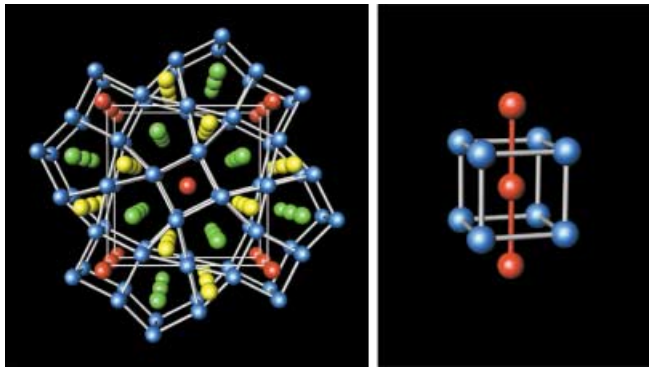

Figure 2. Left: perspective view of the $Mg_2MnRh_5B_2$ crystal structure along the [001] axis with magnesium atoms in green, manganese atoms in red, rhodium atoms in blue, and boron atoms in yellow; right: tetragonal rhodium prisms (blue) around manganese atoms (red).

Magnetic susceptibility measurements on $Mg_2MnRh_5B_2$ immediately revealed Curie–Weiss behavior $\chi_{mol} = C/(T - \Theta_P)$ for temperatures above 160 K with a Weiss constant $\Theta_P = -130$ K and a Curie constant $C = 1.61 \times 10^{-5}$ m^3 K mol^{-1}.[10] The latter number corresponds to a paramagnetic moment of 3.2 μ_B per Mn atom while the former indicates considerable *antiferromagnetic* Mn–Mn exchange interactions. Nonetheless, characteristic features for 1D magnetic behavior are not obvious. Around 3 K, a maximum in χ_{mol} is observed at magnetic fields $B_0 < 0.1$ T. Not too surprisingly, nonmagnetic band-structure calculations on $Mg_2MnRh_5B_2$ fully corroborate the experimental findings. As shown in the left part of Figure 3, the Fermi level in the COHP analysis is clearly positioned in the region of *nonbonding* Mn–Mn interactions, just like in the antiferromagnetic archetype (bcc-Cr). Thus, a tendency for antiferromagnetic spin ordering is indicated by both experiment and theory. To computationally describe this (so far still unknown) antiferromagnetic structure of $Mg_2MnRh_5B_2$ using the simplest model, we doubled the short tetragonal axis and switched to a spin-polarized band-structure calculation. Starting from a rough estimate for the antiparallel spin ordering on the neighboring Mn atoms (ca. $\pm 2\,\mu_B$) and a net moment of zero, the spin-polarized

  1433-7851/02/4114-2529 $ 20.00+.50/0

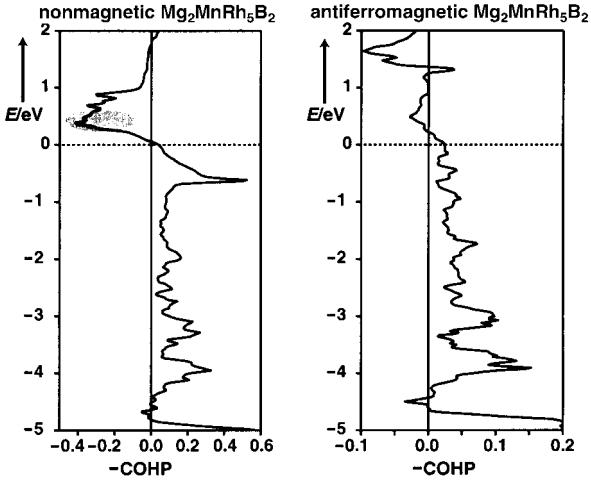

Figure 3. COHP analysis of Mn–Mn bonding in nonmagnetic $Mg_2MnRh_5B_2$ (left) and in antiferromagnetic, spin-polarized $Mg_2MnRh_5B_2$ (right). The Fermi levels (horizontal dotted lines) have been set to zero. The shaded COHP region in the left part symbolizes a hypothetical electronic *enrichment* by three electrons.

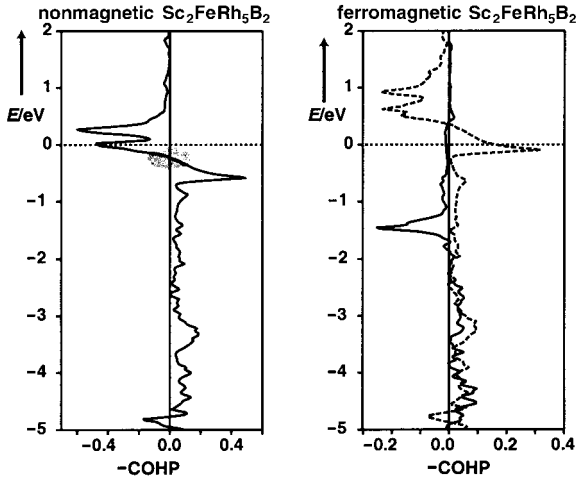

Figure 4. COHP analysis of Fe–Fe bonding in nonmagnetic $Sc_2FeRh_5B_2$ (left) and in ferromagnetic, spin-polarized $Sc_2FeRh_5B_2$ (right). The Fermi levels (horizontal dotted lines) have been set to zero. The shaded COHP region in the left part symbolizes a hypothetical electronic *depletion* by three electrons.

calculation in fact keeps to both the zero net moment and the antiferromagnetic ordering, and it converges to a self-consistent saturation moment of 3.23 μ_B on Mn; all the other atoms are magnetically almost inactive. As expected from the antiferromagnetic archetype (bcc-Cr), in the COHP analysis the nonbonding Mn–Mn states close to the Fermi level (see right part of Figure 3) of the antiferromagnetic calculation remain practically untouched.

Keeping in mind the above-mentioned recipe for synthesizing metallic ferromagnets and antiferromagnets, it is straightforward to predict how to chemically create a new *ferromagnet* starting from the antiferromagnetic $Mg_2MnRh_5B_2$ with 62 valence electrons per formula unit (2×2 (Mg), 1×7 (Mn), 5×9 (Rh), 2×3 (B)). Supposing a rigid-band behavior will hold upon chemical substitution, the experimentalist needs to shift the Fermi level up by increasing the valence-electron concentration such that the new Fermi level will cut through the strongly antibonding states around +0.4 eV as given in the preceding Figure 3 (left, shaded region). A numerical COHP integration shows that such an increase corresponds to *three* additional electrons per formula unit, to be realized by replacing Mg with Sc and Mn with Fe, such that "$Sc_2FeRh_5B_2$" with 65 valence electrons per formula unit (2×3 (Sc), 1×8 (Fe), 5×9 (Rh), 2×3 (B)) should do.[11]

Fortunately, $Sc_2FeRh_5B_2$ can indeed be prepared by classic high-temperature chemical synthesis, similar to the case of the manganese compound.[10] The susceptibility measurement reveals that $Sc_2FeRh_5B_2$ is, in fact, *ferromagnetic* below $T_C = 450$ K. A constant magnetization is easily reached for temperatures below 300 K at applied fields $B_0 > 2$ T with a maximum value of 3.3 μ_B per Fe at 1.7 K. The magnetization above T_C as a function of temperature and applied field is more complicated than would be expected for a simple ferromagnet; Curie–Weiss behavior is not observed. The shape of the corresponding Fe–Fe COHP analysis within a nonmagnetic electronic-structure calculation (see Figure 4, left) is very similar to predictions. In harmony with the ferromagnetic properties of $Sc_2FeRh_5B_2$, there are strongly *antibonding* Fe–Fe interactions around the Fermi level, which remind us of the scenario in the ferromagnetic archetype (bcc-Fe, see above). One may also expect that spin-polarization will remove these antibonding interactions at the Fermi level, thereby lowering the total energy. To do so, the spin-polarized band-structure calculation of $Sc_2FeRh_5B_2$ was started from a small extra moment (ca. 1 μ_B) on the Fe atom and then iterated to self-consistency. As a result, the theoretical saturation moment is 3.96 μ_B while the individual moments (μ_B) are −0.05 for Sc, 2.93 for Fe, 0.25 for Rh1, 0.08 for Rh2, and 0.02 for B. Note that one 4d atom, namely Rh1, is somewhat involved in the magnetic interactions. As predicted, the formerly antibonding Fe–Fe interactions at the Fermi level are no longer visible in a spin-polarized COHP analysis (Figure 4, right), just like for bcc-Fe.

Adopting a similar strategy to that for the antiferromagnetic Mn compound, we can try to plan further synthetic steps on the basis of the non-spin-polarized Fe–Fe COHP analysis of ferromagnetic $Sc_2FeRh_5B_2$ (see again Figure 4, left). It is clear from the Figure that a further electronic *enrichment* will populate more antibonding states which destabilize the structure; in fact, the attempt to increase the valence-electron concentration through substituting Sc atoms by Zr atoms does not lead to alternative ferromagnets but to perovskite-related phases. On the other hand, an electronic *depletion* of ferromagnetic $Sc_2FeRh_5B_2$, for example, by three electrons, would position the Fermi level back into a region of *nonbonding* metal–metal interactions (shaded region in Figure 4, left) which is the fingerprint of an antiferromagnetic material. In other words, a chemical reduction of ferromagnetic $Sc_2FeRh_5B_2$ by three electrons would result in an *antiferromagnetic* alloy, regardless of the magnetic nature of the transition element.

We can come up with two crucial experiments testing the above reasoning, both of which involve a readjusted valence-electron concentration of the intermetallic alloy. In the first

  1433-7851/02/4114-2530 $ 20.00+.50/0

case, we start from the composition $Sc_2FeRh_5B_2$ (65 valence electrons) and lower it by three electrons by substituting Fe for Mn and a partial substitution of Rh for Ru. For example, the hypothetical formula "$Sc_2MnRu_2Rh_3B_2$" with 62 valence electrons per formula unit (2×3 electrons for Sc, 1×7 for Mn, 2×8 for Ru, 3×9 for Rh, and 2×3 for B) would be such a candidate for antiferromagnetism.

As a matter of fact, $Sc_2MnRu_2Rh_3B_2$ can be synthesized by standard methods (see below) in quantitative yields;[12] its magnetization properties are shown in Figure 5. As predicted, the new phase shows *antiferromagnetic* properties, very much resembling isoelectronic $Mg_2MnRh_5B_2$. The Weiss constant Θ_P of $Sc_2MnRu_2Rh_3B_2$ is around -300 K, and the paramagnetic moment corresponds to 2.3 μ_B per Mn atom.

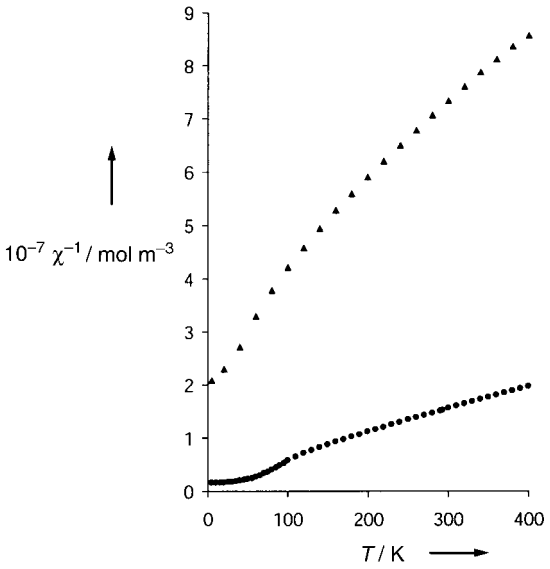

Figure 5. Plots of the reciprocal molar susceptibilities of $Sc_2MnRu_2Rh_3B_2$ (▲) and $Sc_2FeRu_3Rh_2B_2$ (●) as a function of the temperature.

But there is also an alternative way of electronically depleting the 65-electron alloy $Sc_2FeRh_5B_2$, not touching upon the chemical nature of the magnetically active transition metal: To do so, the substitution only involves the Rh sublattice in which *three* of the five Rh atoms are replaced by Ru atoms, thus the synthetic antiferromagnetic target would be "$Sc_2FeRu_3Rh_2B_2$", again corresponding to 62 valence electrons per formula unit (2×3 electrons for Sc, 1×8 for Fe, 3×8 for Ru, 2×9 for Rh, and 2×3 for B).

Fortunately, $Sc_2FeRu_3Rh_2B_2$ is also synthetically accessible in almost quantitative yield.[13] Its magnetic properties (Figure 5) prove that the new material is indeed an *antiferromagnet*, as predicted on the basis of the rigid-band model and the associated COHP diagram. The experimental data reveal that the Weiss constant lies at about -90 K while the paramagnetic moment is 4.0 μ_B per Fe atom. Thus, it is clear that the magnetic type of behavior of both $Sc_2MnRu_2Rh_3B_2$ and $Sc_2FeRu_3Rh_2B_2$ is solely a function of the electron filling, that is, an electron concentration which positions the Fermi level in nonbonding Mn–Mn or Fe–Fe states.

In conclusion, we have exemplified how to understand experimental findings, in terms of the bonding properties of magnetically active transition-metal atoms in complex intermetallic alloys, such as $Mg_2MnRh_5B_2$ and $Sc_2FeRh_5B_2$. We have also shown that the magnetic properties of $Sc_2MnRu_2Rh_3B_2$ and $Sc_2FeRu_3Rh_2B_2$ (and possibly many other intermetallic phases) can be predicted by the shape of COHP diagrams as a function of the electronic energy. From what has been said so far, it seems clear that related, isostructural intermetallic phases with 63 or 64 valence electrons will be interesting candidates for competition between antiferromagnetic (62 electrons) and ferromagnetic (65 electrons) exchange interactions. Corresponding, yet to be synthesized, intermetallic phases with fewer than, say, 62 electrons, should not exhibit strong magnetic phenomena because the Fermi level would be positioned in bonding M–M states in which there is no tendency for electronic distortions in terms of spontaneous spin polarization. Isostructural intermetallic phases with more than 65 electrons are probably impossible to realize synthetically.

Experimental Section and Theoretical Methodology

All intermetallic compounds were synthesized by classic solid-state chemical routes (elemental components, closed containers, high temperatures, and arc melting procedures).[10] The products were structurally characterized by a combination of single-crystal/powder X-ray diffraction and neutron diffraction. The crystallographic lattice parameters of $Mg_2MnRh_5B_2$, $Sc_2MnRu_2Rh_3B_2$, and $Sc_2FeRu_3Rh_2B_2$ were determined from powder. Internal coordinates of $Mg_2MnRh_5B_2$ were assumed to be identical with $Mg_2FeRh_5B_2$ because of their excellent lattice match; these combined spatial parameters were used for the electronic-structure calculation on $Mg_2MnRh_5B_2$. For $Sc_2FeRh_5B_2$, all structural parameters were determined from single-crystal diffractometry and were used, without modification, for the theoretical part. Magnetic susceptibilities were determined between 2 and 400 K at $B_0 = 0.5$ T using a SQUID magnetometer MPMS-5S (Quantum Design, San Diego, USA). Corrections for diamagnetic and conduction-electron contributions were not applied. For $Sc_2MnRu_2Rh_3B_2$ and $Sc_2FeRu_3Rh_2B_2$, the tendency for Curie–Weiss behavior becomes only apparent at $T > 300$ K. This region has thus been used to estimate the corresponding C and Θ_P values.

Band-structure calculations were performed using Linear Muffin–Tin Orbital (LMTO) theory[14] within the local (spin) density approximation (LDA and LSDA).[15] All calculations were checked for convergence of energies, orbital moments, integrated COHP values and magnetic moments with respect to the number of k points used in the reciprocal-space integrations. The program used was TB-LMTO 4.7.[16] Crystal Orbital Hamilton Population (COHP) analysis[17] is a partitioning scheme for the band-structure energy (sum of the energies of the Kohn–Sham orbitals) in terms of orbital-pair contributions. COHP analysis, while in many ways analogous to crystal orbital overlap population (COOP) analysis used in extended Hückel calculations,[18] provides a quantitative measure of bond strengths and is probably more appropriate for a first-principles calculation. All COHP curves are presented here in a format similar to COOP curves: positive values are bonding, and negative antibonding (i.e., we are plotting $-$COHP instead of COHP).

Received: February 18, 2002 [Z18728]

[1] S. Chikazumi, *Physics of Ferromagnetism*, Clarendon Press, Oxford, **1997**.
[2] H. Lueken, *Magnetochemie*, Teubner, Stuttgart, Leipzig, **1999**.
[3] R. C. O'Handley, *Modern Magnetic Materials*, Wiley, New York, **2000**.
[4] R. Dronskowski, *Adv. Funct. Mater.* **2001**, *11*, 27.

[5] G. A. Landrum, R. Dronskowski, *Angew. Chem.* **1999**, *111*, 1482; *Angew. Chem. Int. Ed.* **1999**, *38*, 1390.
[6] G. A. Landrum, R. Dronskowski, *Angew. Chem.* **2000**, *112*, 1598; *Angew. Chem. Int. Ed.* **2000**, *39*, 1560.
[7] Some aspects of the scenario upon onset of magnetism (antibonding character of degenerate highest crystal orbital, symmetry lowering of the underlying wavefunction upon spin polarization) resemble the classic Jahn–Teller case; however, since only electronic coordinates are involved, the term "electronic" Jahn–Teller instability is probably more appropriate.
[8] A. Decker, G. A. Landrum, R. Dronskowski, *Z. Anorg. Allg. Chem.* **2002**, *628*, 303.
[9] In fact, the change in slope of the COHP is similar to what is observed in the classical Peierls distortion of a 1D chain of H atoms. In the present case, however, only electronic coordinates are involved such that the (admittedly questionable) term "electronic" Peierls instability is better suited.
[10] E. A. Nagelschmitz, W. Jung, R. Feiten, P. Müller, H. Lueken, *Z. Anorg. Allg. Chem.* **2001**, *627*, 523.
[11] A perceptive reviewer raised the question whether an alternative *structural* distortion to a nonmagnetic form might also be possible; indeed, such "conventional" distortion could be expected to equally reduce or remove the antibonding M–M states. Nonetheless, we believe that the purely *electronic* distortion through spin polarization is the preferred choice for the ferromagnetic transition metals and their alloys since it is evidently connected with a smaller energetic penalty. If the latter becomes too large, for example, during the attempted electronic enrichment of $Sc_2FeRh_5B_2$ with even stronger antibonding Fe–Fe interactions (see text), the alternative structural distortion takes over.
[12] $Sc_2MnRu_2Rh_3B_2$ lattice parameters from Guinier measurements: $a = 9.3909(5)$ Å, $c = 3.0170(3)$ Å; the structure has also been confirmed from single-crystal data.
[13] $Sc_2FeRu_3Rh_2B_2$ lattice parameters from Guinier measurements: $a = 9.3319(9)$ Å, $c = 3.0101(5)$ Å; a corroborating refinement from single-crystal data has also been performed. There are small traces of an additional phase (probably Ru_4Fe) present in the powdery material; Ru_4Fe has been observed by D. V. Sokol'skii, L. M. Kurashvili, A. F. Burtsev, K. K. Kuzembaev, *Russ. J. Phys. Chem.* **1987**, *61*, 293.
[14] O. K. Andersen, *Phys. Rev. B* **1975**, *12*, 3060; O. K. Andersen, O. Jepsen, *Phys. Rev. Lett.* **1984**, *53*, 2571; "Tight-Binding Approach to Computational Materials Science": O. K. Andersen, C. Arcangeli, R. W. Tank, T. Saha-Dasgupta, G. Krier, O. Jepsen, I. Dasgupta, *Mater. Res. Soc. Symp. Proc.* **1998**, *491*, 3.
[15] U. von Barth, L. Hedin, *J. Phys. C* **1972**, *5*, 1629.
[16] G. Krier, O. Jepsen, A. Burkhardt, O. K. Andersen, The TB-LMTO-ASA program, version 4.7.
[17] R. Dronskowski, P. E. Blöchl, *J. Phys. Chem.* **1993**, *97*, 8617; see also website http://www.cohp.de
[18] T. Hughbanks, R. Hoffmann, *J. Am. Chem. Soc.* **1983**, *105*, 3528.

Catalytic Activity and Poisoning of Specific Sites on Supported Metal Nanoparticles**

Swetlana Schauermann, Jens Hoffmann, Viktor Johánek, Jens Hartmann, Jörg Libuda,* and Hans-Joachim Freund

Typically, heterogeneous catalysts are based on nanometer-sized active particles, dispersed on an inert support material. In many cases it is assumed that the unique reactivities of such surfaces arise from the simultaneous presence of different active sites. On a molecular level, however, knowledge of the reaction kinetics of such systems is scarce (see e.g. refs. [1, 2] and references therein).

Herein, we present first direct evidence for the different activity of coexisting sites on a well-defined supported-nanoparticle system. As a model reaction we choose the decomposition of methanol on well-ordered Pd crystallites. For this reaction system two competing decomposition pathways exist (Figure 1): whereas dehydrogenation to CO

Figure 1. Schematic representation of the supported Pd nanoparticles and the blocking of defect sites by carbon species during methanol decomposition.

represents the dominating reaction channel,[3, 4] slow carbon–oxygen-bond breakage leads to formation of adsorbed carbon and CH_x species.[4–6] With increasing carbon coverage the rate of carbon–oxygen-bond breakage drops rapidly, whereas the kinetics of dehydrogenation is hardly affected. We show that on ordered Pd crystallites these carbon and hydrocarbon species preferentially block defect sites on the particles such as particle edges and steps (see Figure 1). From this, we conclude that activity for carbon–oxygen-bond breakage is

[*] Dr. J. Libuda, Dipl.-Chem. S. Schauermann, Dipl.-Phys. J. Hoffmann, Dr. V. Johánek, Dipl.-Ing. J. Hartmann, Prof. Dr. H.-J. Freund
Fritz-Haber-Institut der Max-Planck-Gesellschaft
Faradayweg 4–6
14195 Berlin (Germany)
Fax: (+49) 30-8413-4309
E-mail: libuda@fhi-berlin.mpg.de

[**] We acknowledge support of this project by the Max-Planck Society and the Deutsche Forschungsgemeinschaft through the Priority Program 1091.

  1433-7851/02/4114-2532 $ 20.00+.50/0